JOURNAL OF GEOPHYSICAL RESEARCH, VOL. 98, NO. C10, PAGES 18,201–18,211, OCTOBER 15, 1993

Excitation of Seiche Observed in a Small Harbor

MICHELE OKIHIRO, R. T. GUZA, AND R. J. SEYMOUR

Scripps Institution of Oceanography, University of California, San Diego, La Jolla

Seiche measured within a small (0.6 by 0.6 km), shallow (12-m depth) harbor is dominated by oscillations in several narrow infragravity frequency bands between approximately 10^{-3} and 10^{-2} Hz. Energy levels within the harbor are amplified, relative to just outside the harbor in 8.5-m depth, by as much as a factor of 20 at the lowest (grave mode) resonant frequency (~10^{-3} Hz) compared to amplifications of roughly 5 at higher resonant frequencies (~10^{-2} Hz). At nonresonant frequencies, energy levels observed inside the harbor are lower than those outside. These amplifications are compared to predictions of a numerical model of seiche excited by linear, inviscid long waves impinging on a harbor of variable depth. The amplification of higher-frequency (~10^{-2}-Hz) seiches is predicted within a factor of about 2. However, at the grave mode (10^{-3} Hz), the observed amplification decreases with increasing swell and seiche energy levels, possibly owing to the sensitivity of this highly amplified mode to dissipation not included in the inviscid model. The energy levels of higher-frequency seiche within the harbor were predicted from the offshore sea and swell spectra by the ad hoc coupling of the linear model for the amplification of harbor modes with a nonlinear model for the generation of bound infragravity waves outside the harbor. The predictions are qualitatively accurate only when the swell is energetic and bound waves are a significant fraction of the infragravity energy outside the harbor.

1. INTRODUCTION

Seiche in a harbor is caused by the amplification of waves at the so-called "natural frequencies." In response to forcing that is broad banded in frequency, oscillations within the harbor at these natural frequencies increase significantly in magnitude before the energy input from the exciting source is balanced by losses such as those owing to friction, flow separation, boundary absorption, and radiation from the harbor mouth. In small harbors which are sheltered from high frequency (~10^{-1}-Hz) sea and swell, the most energetic motions typically have frequencies in the range 10^{-4}-10^{-2} Hz. The oscillatory horizontal displacements caused by these low-frequency oscillations can seriously interfere with harbor operations [e.g., *Wilson*, 1972; *Morison and Imberger*, 1992].

Analytical, numerical, and laboratory models of seiche are typically used to determine, as a function of frequency, the amplification of wave energy within the harbor relative to unit long-wave energy outside (and propagating toward) the harbor. From a suite of logistically feasible designs, the harbor geometry with minimum wave amplification can be determined, but the results are generally used only qualitatively both because of limited field verification of the basic seiche amplification models and because the excitation of long waves outside the harbor is not well understood. Unless the absolute magnitude of the seiche energy is predicted, the "best" design may still be operationally unacceptable.

The majority of past field studies of harbor seiche have been restricted either to comparisons of observed and predicted resonant frequencies [e.g., *Houston*, 1977; *Gerber*, 1986] or to energy ratios between points within or near the mouth of a harbor [e.g., *Lewis et al.*, 1989; *Morison and Imberger*, 1992; *Botes et al.*, 1982, 1984]. Exceptions include *Yamada et al.* [1983], who showed good agreement between the observed and predicted amplification of the grave mode (6.0×10^{-4}-Hz) in a long and narrow (3.8 by 0.5 km), shallow (depth, 5 to 17 m) harbor in Japan. Large discrepancies between observations and predictions at higher frequencies were attributed to the model assumption of constant depth throughout the harbor and offshore areas. Variable depth was included by *Olsen and Hwang* [1971], who studied the amplification at the grave mode (~3.3×10^{-3} Hz) of a small (~0.2 by 0.5 km) shallow (depth, 6 to 17 m) bay in Hawaii. Numerical model amplifications were applied to the sea surface spectrum obtained from pressure measurements about 3.5 km offshore in 165-m depth. The observed energy in the bay was a factor of 4 larger than predicted, even though energy losses were neglected. *Olsen and Hwang* [1971] speculated that the model underpredictions occurred because edge waves with turning points shoreward of the offshore gauge were not accounted for. In the present study we compare predictions of a linear, variable-depth model to amplifications observed between gauges at four locations in Barbers Point Harbor (12-m depth) and a gauge located only a few hundred meters offshore from the harbor mouth in 8.5-m depth (Figure 1).

Tsunamis [e.g., *Matuzawa et al.*, 1933; *Wilson*, 1971], meteorological disturbances [e.g., *Munk et al.*, 1956; *Wilson*, 1972; *Tintoré et al.*, 1988], and internal waves [*Giese et al.*, 1982, 1990; *Giese and Hollander*, 1987; *Chapman and Giese*, 1990] have all been shown to excite harbor seiche, generally of periods longer than O(10 min) (frequencies <~10^{-3} Hz). *Munk* [1949] and *Tucker* [1950] observed low-frequency motions associated with groups of wind waves on an open coast and *Munk* termed these low-frequency waves "surf beat" to evoke their relationship with the beat in the incident wind waves. The wind wave and surf beat energy increased simultaneously, and *Munk* [1949] speculated that wave groups or surf beat somehow caused harbor seiche. Simultaneous increases in offshore swell and lower-frequency harbor seiche energy have subsequently been reported [e.g., *Wilson*, 1957; *Bichkov et al.*, 1970; *Clark*, 1974; *Botes et al.*, 1982; *Kirkegaard and Nielsen*, 1982; *Lopez and Pina*, 1988; *Morison and Imberger*, 1992]. These swell-driven seiches typically have periods of a few minutes or less (frequencies > ~10^{-3} Hz).

Paper number 93JC01760.
0148-0227/93/93JC-01760$05.00

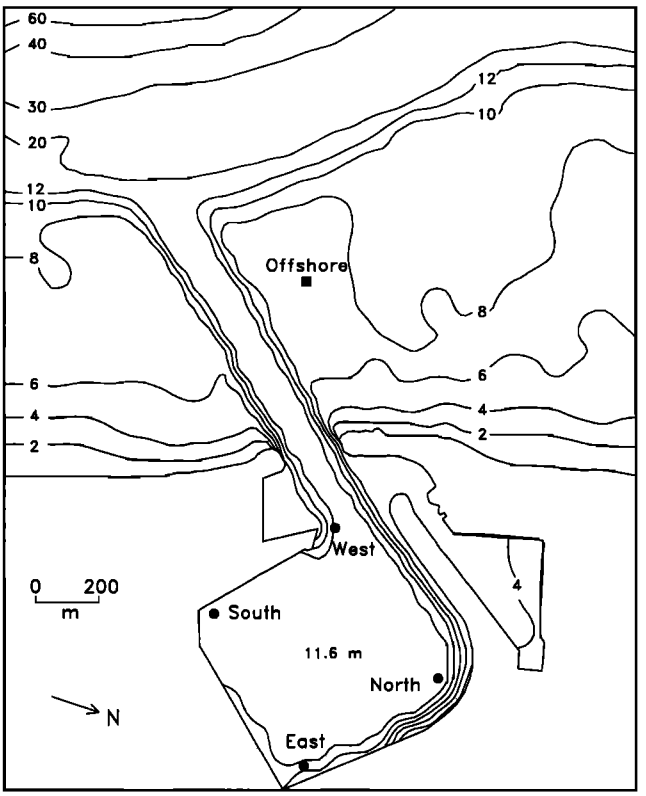

Fig. 1. Instrument positions (solid circles and square indicate sensors within and offshore of the harbor, respectively) and depths (in meters) at Barbers Point Harbor, Oahu, Hawaii.

It has been shown theoretically and in laboratory experiments that groups of swell (and the associated low-frequency bound wave) impinging on a harbor mouth can drive harbor seiche [*Bowers*, 1977; *Mei and Agnon*, 1989; *Wu and Liu*, 1990]. In these models the only free infragravity wave energy outside the harbor is that radiated from the harbor. However, recent observations on open coasts (including sites far from harbors) in depths comparable to the depths of small harbors (i.e., O(10 m)) show that free waves frequently contribute the bulk of the infragravity energy in the swell-driven seiche band (e.g., above roughly 10^{-3} Hz [*Okihiro et al.*, 1992; *Elgar et al.*, 1992; *Herbers et al.*, 1992; Herbers et al., Infragravity-frequency (0.005-0.05 Hz) motions on the shelf, I: Local nonlinear forcing by surface waves, submitted to *Journal of Physical Oceanography*, 1993, hereinafter referred to as Herbers et al. 1993; *Bowers*, 1992]). When swell energy levels are low, no more than a few percent of the total infragravity energy is bound. Bound and free infragravity energy levels are similar only when swell energy levels are relatively high. The energy source and detailed generation mechanisms of free infragravity waves in the swell-driven band is not known, but the waves appear to be generated in very shallow water, perhaps within the surf zone. Energy radiated seaward from shallow water appears to be trapped in the waveguide of the continental shelf by reflection at the shoreline and refraction over the sloping shelf. The trapping does not appear to be highly selective, and observed spectra of free infragravity waves in O(10 m) depth are relatively featureless in frequency and direction (Herbers et al., 1993). Thus, although infragravity waves on the shelf adjacent to the harbor mouth are probably initially generated by nonlinear processes on nearby beaches [e.g., *Munk*, 1949], nonlinear effects (e.g., bound waves) may often be negligible in the harbor [*Wu and Liu*, 1990] and near the harbor mouth. The basic approach taken here is that harbor seiche is the linear response to a directionally broad background of free long waves outside the harbor.

In Section 2, the field site is described and an overview of the observations is given. An existing numerical model [*Chen and Mei*, 1974; *Houston*, 1981; *Chen*, 1984] for seiche caused by linear, inviscid, free waves impinging on a harbor is briefly reviewed in Section 3. In Section 4 the amplifications predicted within the harbor (relative to offshore) are shown to be qualitatively accurate, but in some cases dissipation appears to reduce the observed amplification. In Section 5 we present a crude hybrid model which, by coupling a nonlinear model for infragravity wave generation outside the harbor with the linear harbor seiche amplification model, predicts harbor seiche from the offshore sea and swell spectrum.

2. Field Measurements And Basic Observations

This data set was collected at Barbers Point Harbor (where seiche has sometimes interfered with operations) between October 1989 and March 1990. The main harbor basin is ~0.4 km^2 and 11.6-m deep and is connected to the Pacific Ocean through a 1.3-km-long, 12.8-m-deep entrance channel (Figure 1). The small, shallow (4- to 5-m depth) marina extending northward from the entrance to the main basin was constructed during 1988 and 1989. The coral rock beach in the vicinity of the harbor slopes rather steeply (0.04 slope) from the shoreline to 3-m depth and then slopes more gradually (~0.01) to the 9-m contour (approximately 0.8 km offshore), beyond which the depth increases to 180 m within another 1 km.

Five near-bottom pressure sensors were deployed; four (north, south, east and west, Figure 1) located in the main harbor basin and one (offshore) located in ~8.5-m depth about 200 m north of the entrance channel. Records of 4.6-hour duration were obtained four times a day at a 0.5-Hz sample rate inside the harbor and at 1.0-Hz outside the harbor. The data acquisition system and sensors are described by *Seymour et al.* [1985]. The 508 records when all five sensors were operational were analyzed.

Each 4.6-hour time series record was detrended (with a cubic polynomial) to suppress tidal and other motions with periods greater than the record length. The lowest frequency f considered here is thus roughly 10^{-4}-Hz. Fourier coefficients of pressure calculated from tapered and overlapped 1.1-hour segments were converted to sea surface elevation with linear theory (i.e., at sea and swell frequencies, the attenuation of pressure fluctuations by the water column was accounted for). Power spectra ${}_nG_X(f)$ for each record n and location $X=(x,y)$, obtained by averaging the 1.1-hour segments, have the narrow spectral bandwidth (Δf=2.4x10^{-4} Hz) necessary to resolve the resonant seiche modes but low (about 10) degrees of freedom.

Time histories of wave energy spectra (Figure 2) show that energy outside the harbor at swell frequencies (4.0x10^{-2}-1.5x10^{-1} Hz; Figure 2*a*) is correlated with lower-frequency energy both offshore (Figure 2*b*) and within the harbor (Figure 2*c*). At the offshore location, on average only 1% of the observed total (i.e., sea, swell, and infragravity) energy is at infragravity frequencies (here, 1.0x10^{-4}-4.0x10^{-2} Hz). The relative amount of sea and swell energy varies within the harbor (not shown). For example, the south location is highly sheltered from sea compared to the west gauge (Figure 1), and on average

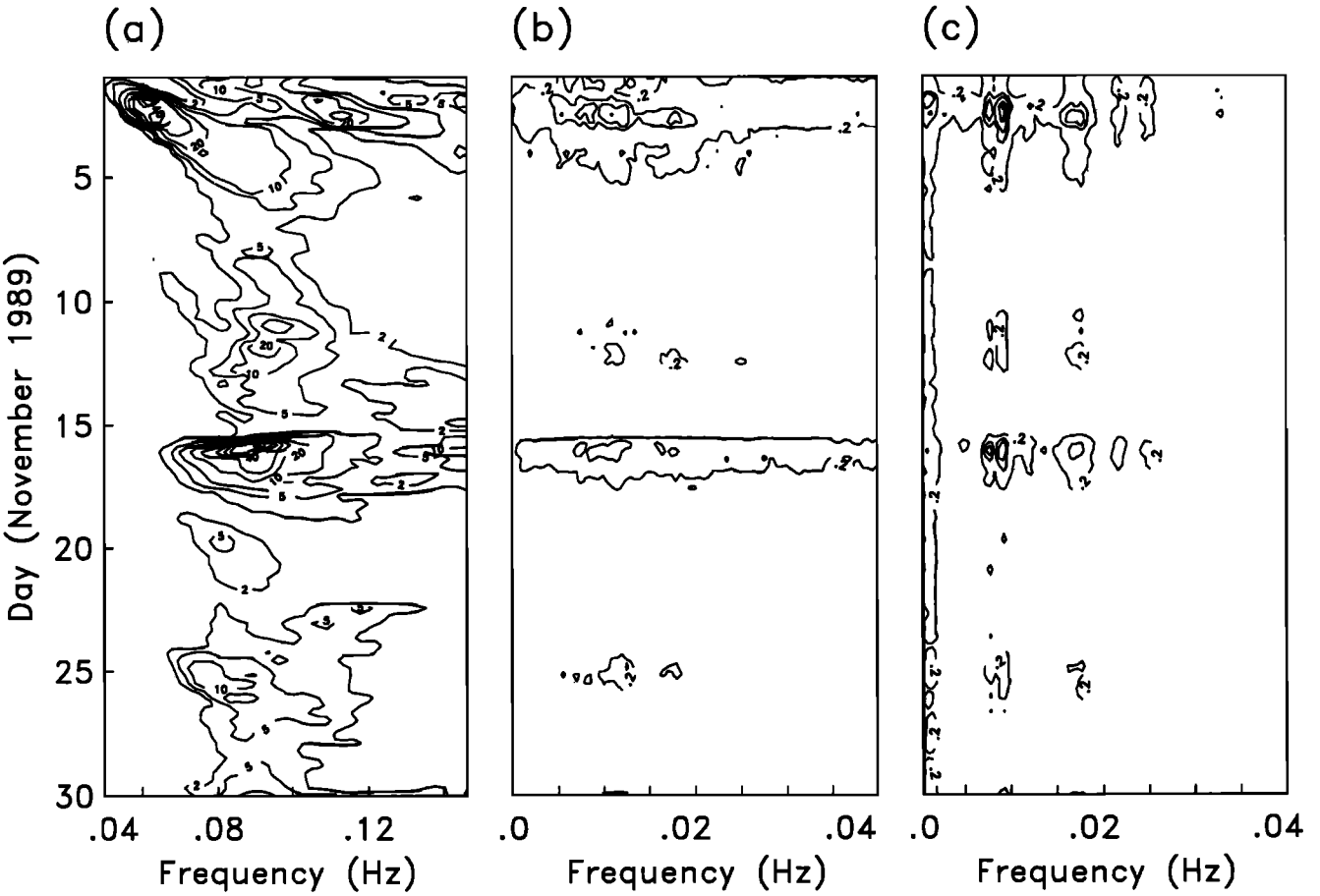

Fig. 2. Contours of wave energy density (units of 10^3 cm^2/Hz) for November 1989 at (*a*) swell frequencies ($4.0\text{x}10^{-2} \leq f < 1.5\text{x}10^{-1}$ Hz) outside the harbor (offshore), (*b*) infragravity frequencies ($10^{-4} \leq f < 4.0\text{x}10^{-2}$ Hz) offshore, and (*c*) infragravity frequencies in the south corner of the harbor. In Figures 2*b* and 2*c*, the contour levels plotted are 0.2, 2, 5, 15, and 25.

15% of the total energy is in the infragravity band at the west gauge, compared to about 50% at the south gauge. The distribution of sea and swell energy within the harbor is not discussed further.

The infragravity energy spectrum ($E_{IG}(f)$) outside the harbor is relatively white, with a smooth increase in the cumulative energy as a function of frequency. In contrast, $E_{IG}(f)$ within the harbor is elevated in narrow frequency bands corresponding to the resonant modes of the harbor, where there are step increases in the cumulative energy (Figures 3*a* and 3*b*). On average, ~75% of the total infragravity energy in the harbor is at frequencies of less than $1.2\text{x}10^{-2}$ Hz, the highest infragravity frequency considered in the model-data comparisons (section 4). The observed power at the lowest resonant frequency, the grave or Helmholtz mode at 10^{-3} Hz, is approximately equal at different locations in the interior of the harbor, with the lowest level at the west location in the entrance channel (Figure 3*a*). The energy levels of resonant modes at higher frequencies are more variable within the harbor, but all locations have multiple peaks between $5.0\text{x}10^{-3}$ and $9.0\text{x}10^{-3}$ Hz.

The correlation between infragravity $E_{IG}(f)$ and total offshore swell energy (E_{SWELL}, the energy integrated over the $4.0\text{x}10^{-2}$-$1.5\text{x}10^{-1}$ Hz swell band) typically varies as a function of infragravity frequency f [*Munk et al.*, 1956; *Donn and McGuinness*, 1963; *Morison and Imberger*, 1992; *Herbers et al.*, 1992] and in the present observations (Figure 3*c*) is low for frequencies of less than about $2.0\text{x}10^{-3}$ Hz. At frequencies below about $2.0\text{x}10^{-3}$ Hz, which includes the grave mode (10^{-3} Hz), infragravity motions may be driven by atmospheric processes [e.g., *Munk et al.*, 1956] as illustrated in Figure 4. Coincident with an atmospheric pressure drop of 17 mbar, the energy of grave mode oscillations increased by roughly an order of magnitude (there were no significant increases in sea and swell energy). It is not clear whether the harbor seiche was driven by direct meteorological forcing of the harbor or by long waves on the shelf which were excited by the frontal passage. Other processes (e.g., internal waves and tsunamis) may also force the grave mode at Barbers Point.

Seiche energy was split into broad frequency bands corresponding to the different dominant forcing mechanisms. The lower-frequency, grave mode band extends from about 10^{-4} Hz (the lowest resolved frequency) to $2.0\text{x}10^{-3}$ Hz (approximately the transition to seiche driven by local swell; Figure 3*c*). A second frequency band spans the range $2.0\text{x}10^{-3}$-$1.2\text{x}10^{-2}$ Hz, and the third band (not included in model-data comparisons; section 4) extends from $1.2\text{x}10^{-2}$-$4.0\text{x}10^{-2}$ Hz. Energy levels of both of these higher-frequency seiche bands are strongly correlated with the total swell energy (Figure 3*c*).

Outside the harbor (Figure 5*a*), the grave mode band is not as energetic as the higher-frequency seiche bands. Within the harbor, the grave mode dominates the seiche energy when the swell energy (E_{SWELL}) is low, but when the swell is energetic,

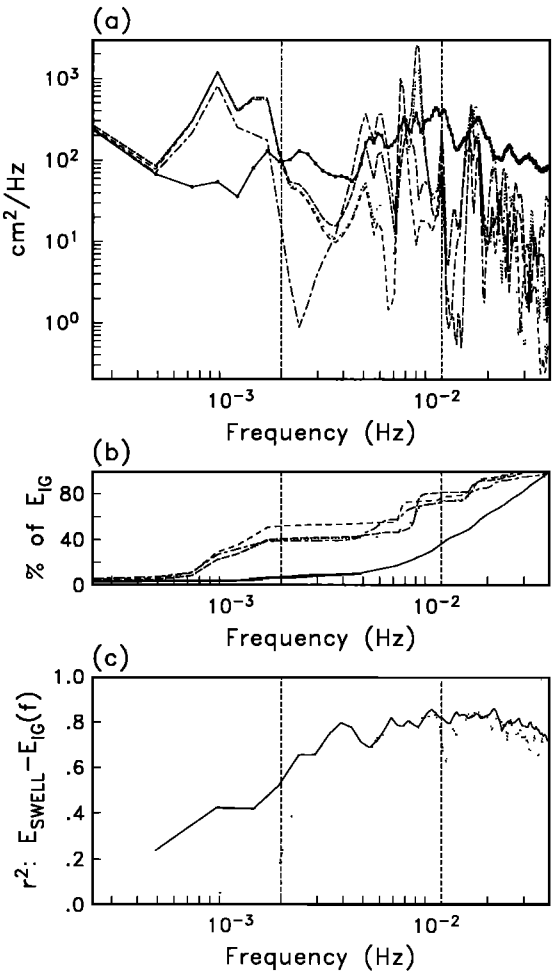

Fig. 3. (*a*) Average observed power spectra and (*b*) average cumulative percentage of the total infragravity energy; offshore (solid line) and in the harbor (south, dotted line; north, short-dash line; west, dot-dash line; east, long-dash line). (*c*) Correlation (r^2) between the logarithms of the total swell energy E_{SWELL} and offshore infragravity energy $E_{IG}(f)$ as a function of f (solid line) and the average r^2 between E_{SWELL} and $E_{IG}(f)$ at the four harbor gauges (dotted line). The dashed vertical lines at 2.0×10^{-3} and 1.2×10^{-2} Hz delineate frequency bands discussed in the text.

the higher-frequency seiche modes contribute the bulk of the infragravity energy (Figure 5*b*). The differential amplification which increases the importance of the grave mode inside the harbor (relative to that outside the harbor) is apparent in Figure 6. The grave mode band is amplified by a factor of roughly 2-10, whereas the next higher-frequency band is usually slightly less energetic inside the harbor than outside, and the highest infragravity band typically has only 20-40% of the energy outside the harbor.

The experiment-averaged energy amplification (as a function of frequency) $\langle A(X_2,X_1,f)\rangle$ at location X_2 relative to X_1 is defined as the average of the ratios of the smoothed power spectra G from all (N=508) individual 4.6-hour records (there are small differences between the average and the median ratio),

$$\left\langle A(X_2,X_1,f)\right\rangle = \frac{1}{N}\sum_{n=1}^{N} {}_nG_{X_2}(f)/{}_nG_{X_1}(f). \qquad (1)$$

Peaks in $\langle A(X_2,X_1,f)\rangle$ may result from either peaks (i.e., resonances) in ${}_nG_{X_2}(f)$ or depressions (i.e., nodes) in ${}_nG_{X_1}(f)$. However, because the average power spectrum outside the harbor is relatively white (compared with the power spectra in the harbor; Figure 3*a*) over much of the infragravity frequency band, the structure of the energy amplification spectra (between the offshore and all harbor locations; Figure 7*a* is typical) is primarily due to the frequency structure of the power spectra in the harbor. The approximately unity transfer function between the south harbor and offshore sites in the 2.0×10^{-3}- to 1.2×10^{-2}-Hz band (Figure 6) results from an approximate balance between amplification of two peaks at ~8.0×10^{-3} Hz (Figure 7*a*) and strong suppression of seiche energy at other frequencies in this band. The grave mode band is amplified across the entire bandwidth (with peak amplifications of about 20), whereas the highest seiche frequency band is amplified only slightly in a narrow band around 1.7×10^{-2} (Figures 3*a* and 7*a*).

Experiment-averaged cross spectra were computed using a variance normalization [*Munk et al.*, 1964] which essentially equally weights the cross spectra of each data record. Examples of experiment-averaged phase differences between sensor pairs obtained from these cross spectra are shown in Figure 7*b*.

Amplification spectra (equation (1)) and normalized cross spectra were separately averaged over "energetic" and "calm" records (defined as E_{SWELL}>625 cm^2 and E_{SWELL}<156 cm^2 outside the harbor, respectively) as well as over all records (Figure 7). Although there are detectable differences between energetic and calm records (e.g., the amplification at the grave mode tends to be less when the swell is energetic; Figures 6 and 7), the overall patterns of energy amplifications and phase differences (between offshore and harbor locations) for the E_{SWELL} separated data are certainly similar. The observations are not obviously inconsistent with the assumption (section 3) that the spatial structure (amplification and phase differences relative to those offshore) of harbor seiche can be described with linear dynamics.

The observed frequencies and energy levels of peaks in the infragravity power spectra of harbor seiche are slightly different at low and high tides (depth differences of 0.9 m or less). Although detectable, these tide-induced changes are relatively small, and no distinction will be subsequently made according to tidal stage. Numerical model calculations (section 3) use the mean tide level.

A limited amount of data from a few sensors was collected prior to construction of the small shallow marina to the

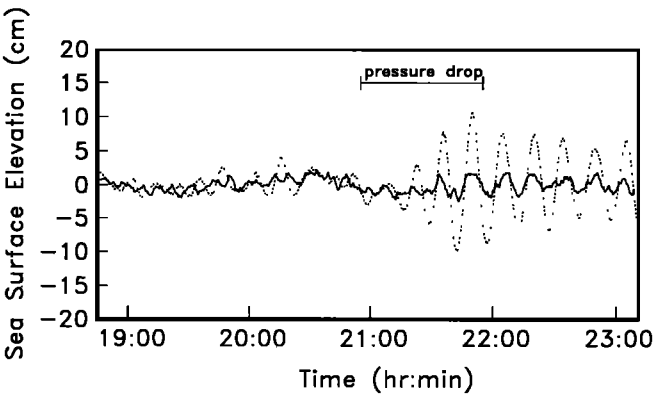

Fig. 4. Low-pass-filtered (2-min average) sea surface elevation time series on December 11, 1987, offshore (solid line) and in the south corner (dotted line). The atmospheric pressure dropped 17 mbar during the time indicated, and the grave mode energy (period, ~15 min) increased dramatically.

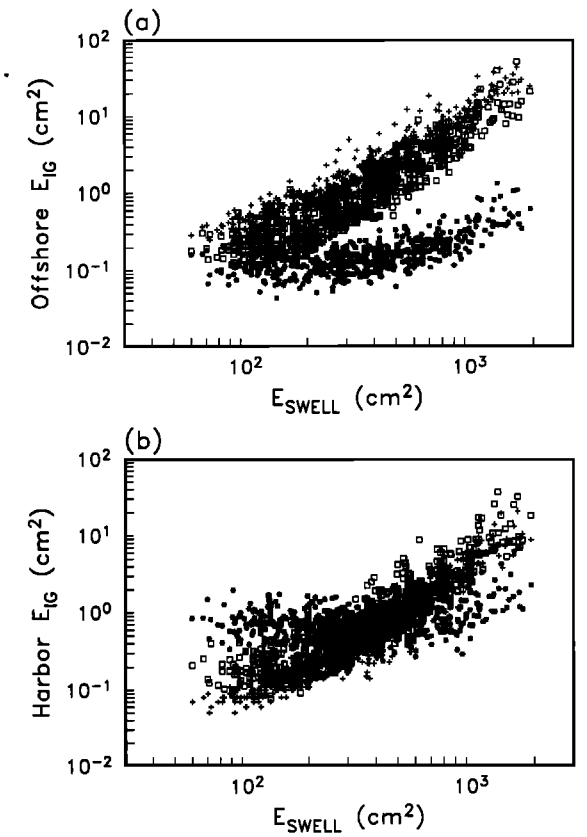

Fig. 5. Infragravity energy (E_{IG}) versus offshore swell energy (E_{SWELL}) at the (*a*) offshore and (*b*) south corner. E_{IG} is the total energy in the following frequency bands: $10^{-4}\leq f<2.0\text{x}10^{-3}$ Hz (asterisks), $2.0\text{x}10^{-3}\leq f<1.2\text{x}10^{-2}$ Hz (squares), and $1.2\text{x}10^{-2}\leq f<4.0\text{x}10^{-2}$ Hz (pluses).

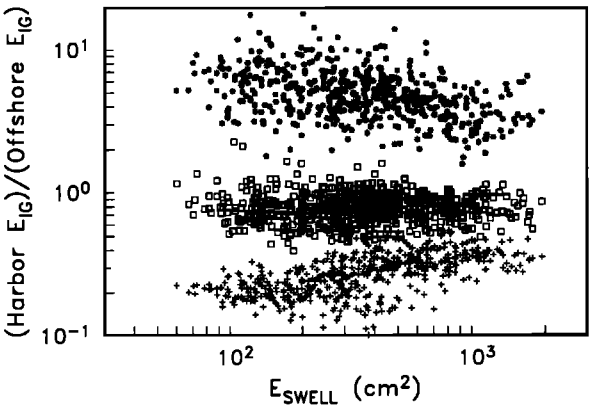

Fig. 6. Ratio between infragravity energy measured in the south corner and offshore. The frequency ranges spanned by E_{IG} are $10^{-4}\leq f<2.0\text{x}10^{-3}$ Hz (asterisks), $2.0\text{x}10^{-3}\leq f<1.2\text{x}10^{-2}$ Hz (squares), and $1.2\text{x}10^{-2}\leq f<4.0\text{x}10^{-2}$ Hz (pluses).

northwest (Figure 1). Comparison of pre- and post-construction amplification spectra at the west corner (dashed and solid lines in Figure 11*a*) show that the marina introduced a node at $7.0\text{x}10^{-3}$ Hz but did not otherwise significantly alter the amplification spectra.

3. NUMERICAL MODEL

Model Description

The numerical model used here is the solution of a boundary value problem for linear gravity waves in a domain of arbitrary shape and variable depth [*Chen and Mei*, 1974; *Houston*, 1981; *Chen*, 1984]. The governing equation is [*Berkhoff*, 1972]

$$\nabla\cdot(bcc_g\nabla\phi)+\frac{\omega^2 c_g}{c}\phi=0 \qquad (2)$$

where ∇ is the horizontal gradient operator; ϕ is the velocity potential; c and c_g are the phase velocity and group velocity, respectively; ω is the radian frequency ($\omega=2\pi f$); g is gravity; and $\omega^2=gk\tanh(kh)$, with k the wave number and h the depth. Energy losses from bottom friction are parameterized in b, where $b=[1/(1+(\beta i a_o e^{i\pi/4}\,)/(h\,\sinh(kh))]$ and a_o is a typical incident wave amplitude. Equation (2) is the inviscid mild-slope equation when the bottom friction coefficient $\beta=0$ and $b=1$.

The solution domain is divided into variable-depth near-regions H and A and a constant-depth far-region R, separated by an artificial semicircular boundary ∂A where solutions are matched and a Sommerfeld radiation condition is satisfied (Figure 8). The solution in regions H and A is found using finite-element techniques, while the solution in R is analytic.

The dissipative effects of incomplete reflection at boundaries and bottom friction can be included in the numerical model, but values for coefficients must be empirically (or arbitrarily) chosen. We neglect dissipation and thus quantify the differences between observed energy amplifications and predictions of a linear inviscid model with no free parameters. The no-flow boundary condition (i.e., $\partial\phi/\partial n=0$, $n=0$, n is unit normal vector) is satisfied along the periphery of the harbor and

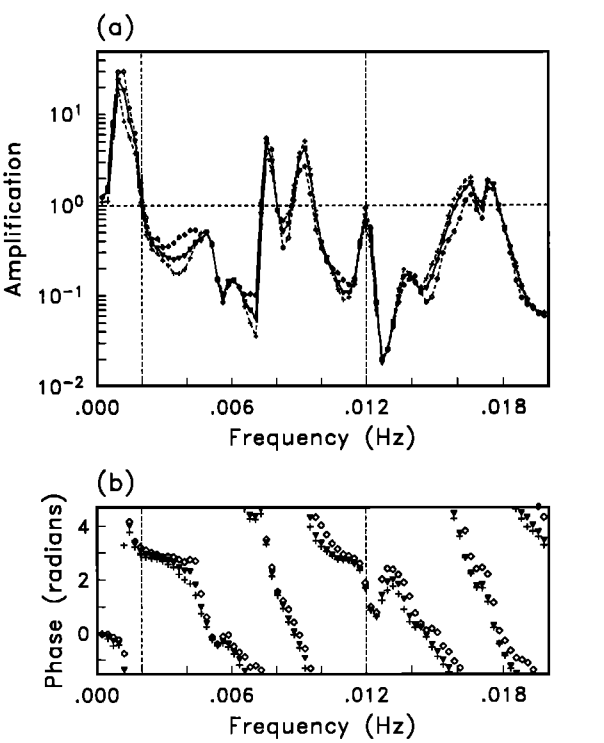

Fig. 7. South corner relative to offshore (*a*) energy amplification (dashed horizontal line is unit amplification) and (*b*) phase averaged over all data (solid line and triangles), calm (E_{SWELL} < 156 cm^2) records (dashed line and diamonds), and energetic (E_{SWELL} > 625 cm^2) records (dashed line and pluses).

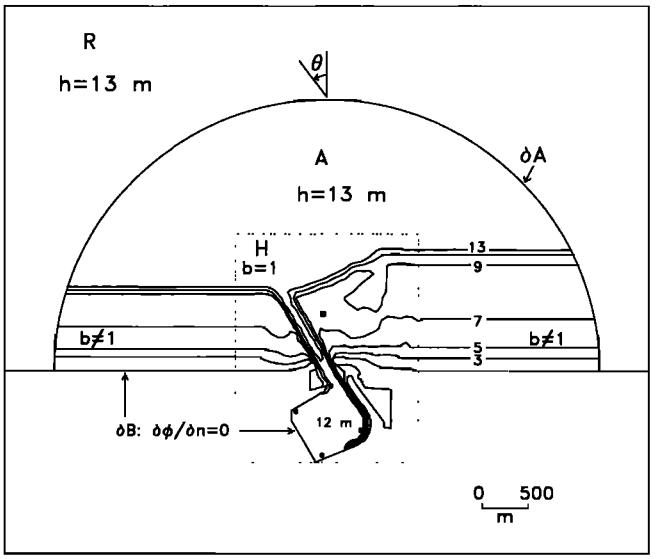

Fig. 8. Definition sketch of the harbor model regions (R, A, and H), boundaries (∂A and ∂B), depths (h), bottom friction (b), and incident wave direction (θ). Harbor and offshore sensors are shown by solid circles and a square, respectively. The measured bathymetry in region H (dotted box) is shown in Figure 1.

surrounding coasts (∂B, Figure 8), and bottom friction is neglected (i.e., β=0 and b=1) in the harbor and nearshore area of interest (region H).

Undesirable wave reflection, refraction, and scattering occur at the depth discontinuity on the semicircular boundary ∂A between the variable-depth near-region A and constant-depth far-region R (Figure 8). The location of ∂A and the values of bottom friction in region A effective in reducing these model artifacts were determined empirically on bathymetry with known analytical solutions for a range of infragravity frequencies. The effect of depth discontinuities was reduced by placing ∂A where the actual bathymetry is relatively smooth and planar and selecting the constant far-region depth (here, 13 m) to match the measured bathymetry over a large portion of ∂A (Figure 8). However, where ∂A intersects the shoreline, the depth still changes abruptly from zero in region A to 13 m in the far-field R. To further reduce the bogus effects of these depth discontinuities, nonzero and spatially variable bottom friction (β values between 10^{-5} and 10^{-3}) was specified near the boundary between the coast and ∂A (Figure 8). Bottom friction was included in less than 5% of the total grid area, and the results in region H were not sensitive to the details of the damping. The radius of region A ranged from 2 to 3 km, and ∂A was therefore less than one wavelength distant from the harbor mouth for the lowest frequencies considered and several wavelengths away for the higher infragravity frequencies. The grid size was constrained by the available computer time. The approximately 20,000 triangular elements in each grid had dimensions (typically 18-45 m) much less than the local wavelength. Various numerical tests indicated that boundary and other model artifacts are smaller than the discrepancies with observations discussed in section 4.

Model Results

The model output used here is the complex free surface displacement $\eta(X,f,\theta)$ at location X relative to a monochromatic unidirectional wave of unit amplitude and incident direction θ (Figure 8) in the far-field. The amplification at X relative to shoreward propagating waves with unit energy in the far-field (∞) is

$$A(X,\infty,f,\theta) = |\eta(X,f,\theta)|^2. \quad (3)$$

The directions of low-frequency waves (at Barbers Point) were unknown, but the model amplifications (both inside and just outside the harbor) are only weakly sensitive to θ. To approximate the broad directional distribution of infragravity energy measured in comparable depths at other sites (Herbers et al., 1993), model amplifications $A(X,\infty,f,\theta)$ were calculated for five far-field directions θ ranging from -30° to 30°. To resolve the sharp resonant peaks, the model was tested with frequency resolution as fine as 3.8×10^{-6} Hz. A smoothed model spectrum of energy amplifications is obtained by averaging monochromatic results over all directions and over frequency [e.g., *Panchang et al.*, 1990] to match the frequency resolution (2.4×10^{-4} Hz) of the field data. Owing to limitations on computer time, model results were obtained only for frequencies less than 1.2×10^{-2} Hz. Model results are cast as smoothed, energy amplification spectra between locations X_1 and X_2

$$\langle A(X_2,X_1,f)\rangle = \frac{\langle A(X_2,\infty,f)\rangle}{\langle A(X_1,\infty,f)\rangle}. \quad (4)$$

Figure 9 shows $\langle A(X_2,X_1,f)\rangle$ with X_2=south and X_1=offshore sensor positions (Figure 1), and also the energy amplification spectra relative to infinity ($\langle A(\text{south},\infty,f)\rangle$ and $\langle A(\text{offshore},\infty,f)\rangle$). Normalizing the model predictions within the harbor by the wave field at the offshore sensor has a small effect, for example, shifting the grave mode peak a single frequency band from 9.8×10^{-4} in $\langle A(\text{south},\infty,f)\rangle$ to 1.2×10^{-3} Hz in $\langle A(\text{south,offshore},f)\rangle$.

Examples of the spatial structure of the smoothed energy amplification relative to the offshore sensor (Figure 1) are

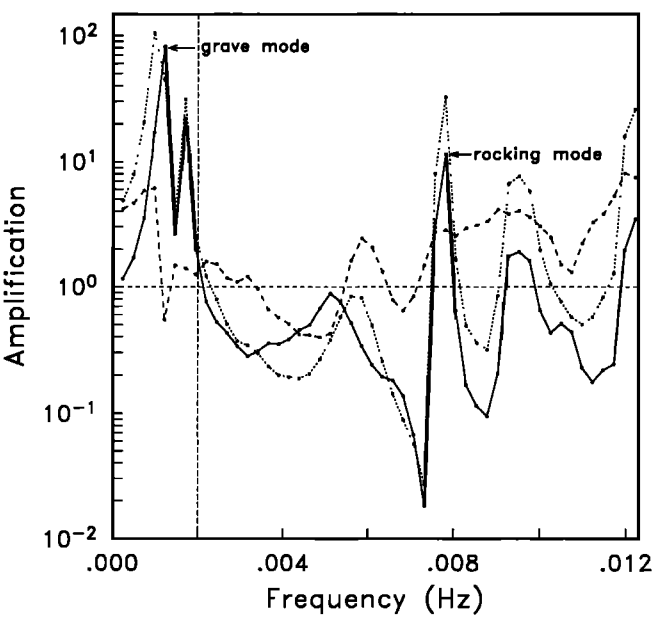

Fig. 9. Model-predicted energy amplification spectra smoothed over frequencies and directions. Solid line is $\langle A(\text{south,offshore},f)\rangle$, dashed line is $\langle A(\text{offshore},\infty,f)\rangle$, and dotted line is $\langle A(\text{south},\infty,f)\rangle$. The spatial structures of the grave and rocking modes are shown in Figures 10*a* and 10*b*, respectively.

shown in Figure 10 for two resonant frequencies. Figure 10*a* shows the grave mode (1.2×10^{-3} Hz) with relatively uniform amplifications (50-90) in the main harbor interior, decreasing amplification along the entrance channel toward the harbor mouth (qualitatively consistent with the relatively low power observed at the west gauge; Figure 3*a*), and a nodal line near the offshore sensor. Note the strong amplification (200) predicted in the (uninstrumented) shallow (depth, ~5 m) marina extension. At higher resonant frequencies, the patterns of wave energy amplification are more complex. Figure 10*b* illustrates a "rocking mode" with a nodal line across both the main basin and marina. Model phase predictions (discussed below) were obtained from frequency- and θ direction-averaged model cross spectra.

4. MODEL-DATA COMPARISONS

The frequencies of peaks and valleys in the observed experiment-averaged energy amplification spectra (equation (1)) and the phase differences between the harbor and offshore locations are well predicted (Figure 11). However, there are significant differences in the magnitudes of the resonant peaks (e.g., the amplification of the grave mode is on average overpredicted at all four gauges). Similar comparisons, but between the south and west harbor gauges are shown in Figure 12. The peaks in the amplification spectra result from both spectral maxima at the south gauge and minima at the west gauge (Figure 3*a*). The predicted 0, π phase differences between the harbor gauges are observed both with high and low offshore swell energies. The agreement between all pairs of harbor gauge locations is similar to that in Figure 12.

The slight offset of the predicted amplification maxima to higher frequencies than observed (Figures 11 and 12) may be the result of erroneous model depths. A 1-m-thick accumulation of sediment in parts of the harbor between the bathymetric surveys (1985) and the present measurements (1989-1990) could account for the observed frequency offset (about 1 or 2 frequency bands). Nonlinear effects [e.g., *Rogers and Mei*, 1978; *Lepelletier and Raichlen*, 1987] can also shift the resonant frequency, but nonlinearity is probably weak within the harbor because both swell and seiche amplitudes are relatively small. For example, there is no evidence of nonlinearly generated harmonics of the grave mode (e.g., Figure 3), as occurs with sufficiently energetic seiche in numerical simulations [*Rogers and Mei*, 1978].

Observed experiment-averaged energy amplification and phase spectra are compared to predictions in Figures 11 and 12. Observed and predicted amplifications of frequency-band-integrated energy for all 508 individual records are shown for the offshore and south gauge pair in Figure 13. The observed amplification of the grave mode, roughly 2-10 (Figure 6), is slightly overpredicted when swell energy is low but overpredicted by a factors of 4-6 when swell energy is highest (Figure 13*a*). This is the case for the grave mode band for all four harbor sensors. At the next higher-frequency infragravity band, where the observed amplification is between 0.5 and 1 (Figure 6), the model overpredicts the amplification by roughly a factor of 2 at the south (Figure 13*b*), north, and west (not shown) gauges independent of swell energy. Curiously, the amplification of the higher-frequency infragravity band at the east gauge (not shown) is underpredicted both with increasing swell and on average (e.g., the average underprediction of the

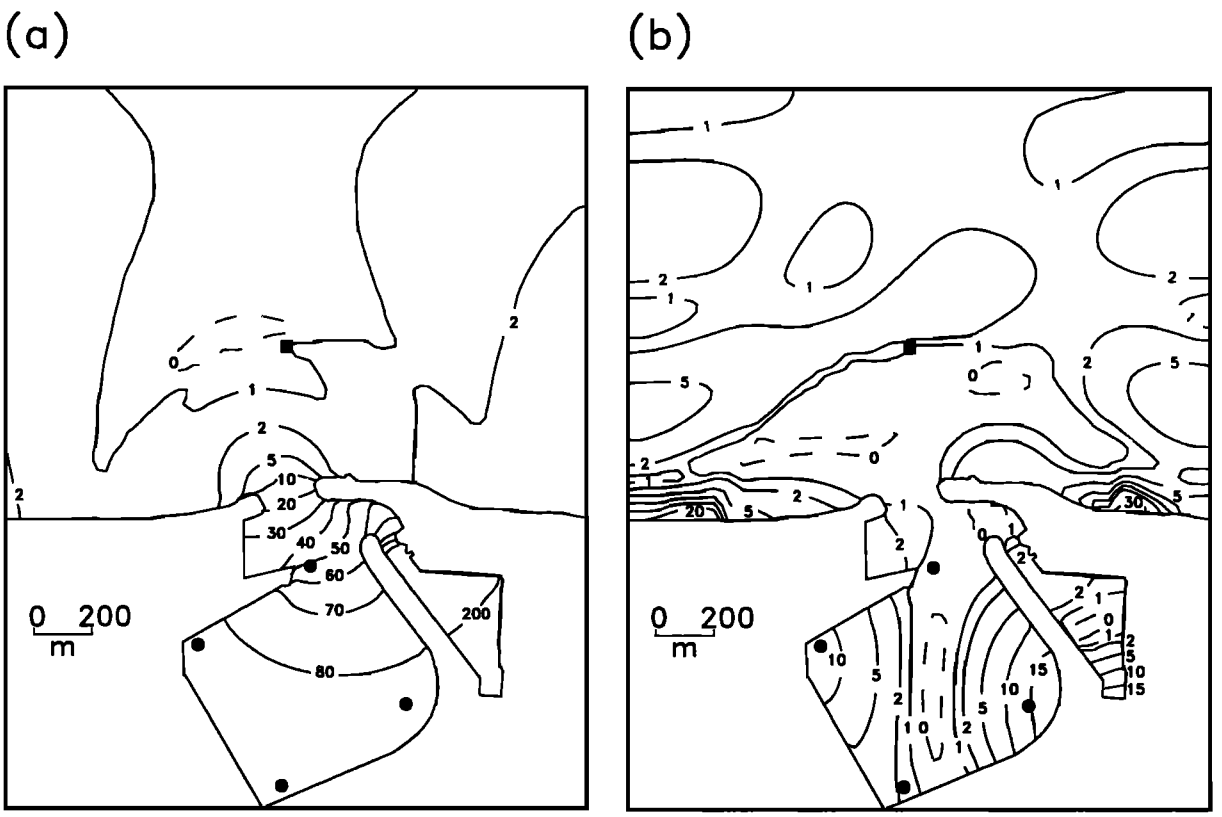

Fig. 10. Contours of model-predicted wave energy for unit energy at the offshore sensor position (square) for the (*a*) grave mode, f=1.2×10^{-3} Hz, and (*b*) rocking mode, *f*=7.8×10^{-3} Hz. The dashed lines are amplifications ~0. Solid symbols indicate sensor positions.

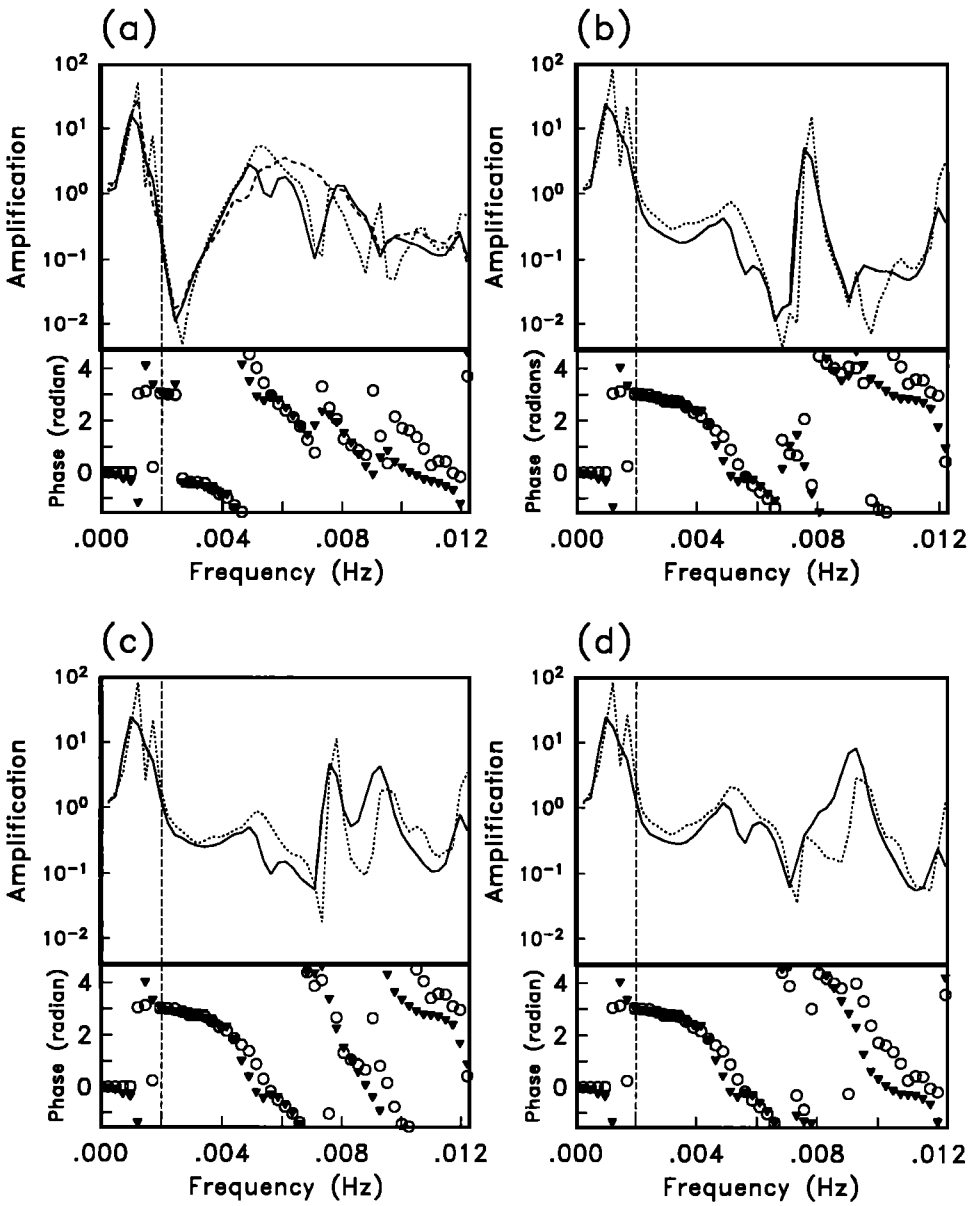

Fig. 11. Model-predicted (dotted line and circles) and observed (solid line and triangles) energy amplification and phase between the offshore location and (*a*) west corner, (*b*) north corner, (*c*) south corner, and (*d*) east corner of the harbor. The dashed line in Figure 11*a* is the observed energy amplification before the marina northwest of the main basin was added to the harbor (see section 2).

peak observed at ~9×10^{-3} Hz in Figure 11*d* occurs for high and low swell energy).

Energy dissipation owing to friction, flow separation near the harbor mouth, and incomplete reflection at boundaries was neglected in the model and may cause the consistent model overpredictions of the grave mode amplification (Figures 11 and 13*a*). Even small deviations from perfect boundary reflection can cause large overpredictions of resonant amplification [*Ippen and Goda*, 1963; *Kostense et al.*, 1986]. Energy losses at the harbor entrance also reduce the energy amplification, particularly for the grave mode, where the predicted amplification is high [*Ito*, 1970; *Horikawa and Nishimura*, 1970; *Lee*, 1971; *Ünlüata and Mei*, 1975; *Bowers*, 1977; *Lepelletier*, 1980; *Zelt*, 1986]. Trends in the present results are qualitatively consistent with dissipative effects. The overprediction of the grave mode amplification is larger than for the less amplified high-frequency band, and overpredictions of the grave mode increase when swell and infragravity energy (and nonlinear frictional losses) are largest. It is possible to heuristically introduce energy losses by setting $b \neq 1$ in equation (2) or to allow incomplete boundary reflection, but there is no a priori way to determine the coefficient values.

A reviewer suggested that the overpredicted amplification at resonant modes could also occur because the observations at the offshore location include contributions from free waves generated at the harbor mouth by the discontinuity of bound long waves [*Bowers*, 1977; *Mei and Agnon*, 1989; *Wu and Liu*, 1990]. This effect is neglected in the linear model.

5. FORCING OF HARBOR SEICHE BY SEA AND SWELL

The energy level in the grave mode frequency band is not in general related to swell energy outside the harbor (Figure 3*c*).

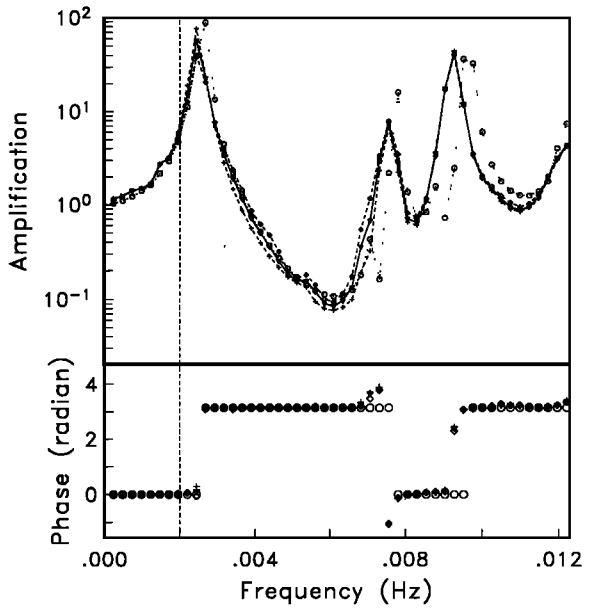

Fig. 12. Model-predicted (dotted line and circles) and observed energy amplifications (ratios) and phases between the south and west locations in the harbor. Observed data are averaged over all data (solid line and triangles), calm (E_{SWELL} < 156 cm^2) records (dashed line and diamonds), and energetic (E_{SWELL} > 625 cm^2) records (dashed line and pluses).

Only when the swell energy is nearly maximum is there a detectable elevation of grave mode energy above a background level (Figure 5) which is apparently forced by atmospheric (Figure 4) and other processes. On the other hand, the higher-frequency (2.0×10^{-3}-4.0×10^{-2} Hz) seiche energy is highly correlated with swell energy (Figures 3*c* and 5). The coupling between swell and high-frequency (>10^{-3} Hz) long waves outside Barbers Point Harbor was investigated in detail by *Okihiro et al.* [1992] using a different data set [see *Elgar et al.*, 1992]. The frequency directional spectra $E(f,\theta)$ of sea and swell (i.e., f>4.0×10^{-2} Hz) were estimated using measurements from a 6 by 6 m array of four pressure sensors at the location of the present offshore sensor (Figure 1). The $E(f,\theta)$ estimates were used to predict the bound wave spectra below 4.0×10^{-2} Hz, using weakly nonlinear theory [*Hasselmann*, 1962]. When the swell energy was low, bound wave model predictions were typically less than 10% of the observed infragravity energy levels. However, nearly half the total infragravity energy in 8.5-m depth was estimated to be bound with energetic swell (E_{SWELL}≥2000 cm^2). The accuracy of the bound wave predictions was limited by the low directional resolution of the small array, but more accurate results obtained with high-resolution estimates of $E(f,\theta)$ from a large-aperture, 24-element array deployed at Duck, North Carolina [*Herbers et al.*, 1992, 1993], are qualitatively similar.

Predictions of infragravity bound waves at the offshore array were made for the small subset (i.e., 26 records) of the present data when the four-element offshore array [*Okihiro et al.*, 1992] was operational. The offshore swell energy E_{SWELL} for the reduced data set spanned the range 100 to 2000 cm^2, nearly the same as the present total data set (e.g., Figure 5). Figure 14 shows predicted bound wave and observed offshore infragravity energy for the portion of the swell-driven infragravity frequency band for which harbor seiche model predictions are available (2.0×10^{-3}-1.2×10^{-2} Hz). As with the larger data set used by *Okihiro et al.* [1992], only a small fraction of the observed infragravity energy E_{IG} at the offshore location is bound when E_{SWELL} and E_{IG} are small. Models for harbor seiche which do not include forcing by free waves outside the harbor will necessarily perform poorly in these cases. However, bound waves contribute nearly half of the total infragravity energy when the swell is energetic.

The bound wave model predicted infragravity spectra at the offshore location were used as input to the linear harbor seiche model (section 3). That is, the predicted bound infragravity wave spectrum at the offshore sensor was used instead of the observed offshore infragravity spectrum as in Figures 11-13. For low E_{IG} (and E_{SWELL}), the bound wave model severely underpredicts the harbor seiche (Figure 15), probably because infragravity energy offshore of the harbor is grossly underpredicted (Figure 14).

The harbor seiche energy levels predicted using the observed offshore energy levels (as in Figures 11-13) are also shown in Figure 15. As in the entire data set (Figure 13b), predictions for this reduced data set are biased high by less than a factor of 2 for all infragravity (and swell) energy levels. For the highest E_{IG} (and E_{SWELL}), both seiche predictions (e.g., using the observed $E_{IG}(f)$ and the bound wave model predicted $E_{IG}(f)$) are within a factor of 2 of the observed values, though the errors are of different signs. For these few cases, the harbor seiche can be predicted about as accurately from the offshore sea and swell

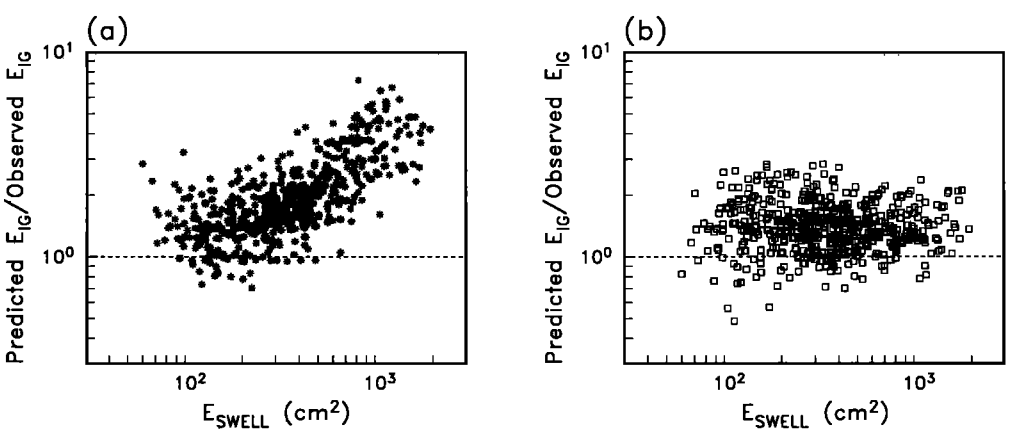

Fig. 13. Ratios of predicted and observed energy in the south corner versus offshore total swell energy (E_{SWELL}). The frequency ranges spanned by E_{IG} are (*a*) 10^{-4}≤f<2.0×10^{-3} Hz (asterisks) and (*b*) 2.0×10^{-3}≤f<1.2×10^{-2} Hz (squares).

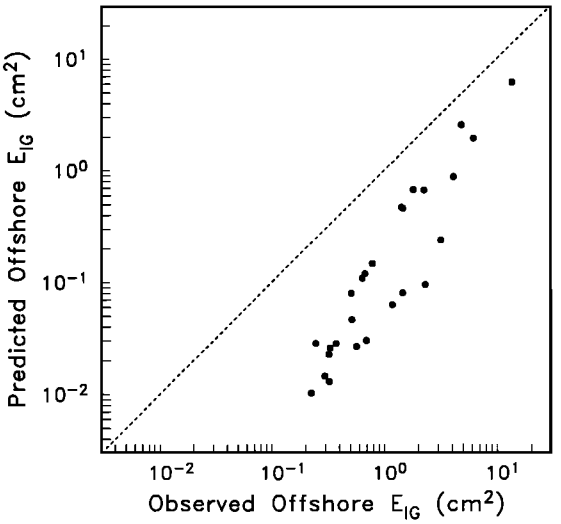

Fig. 14. Predicted (bound-wave model) versus observed infragravity energy ($2.0x10^{-3} \leq f < 1.2x10^{-2}$ Hz) at the offshore location.

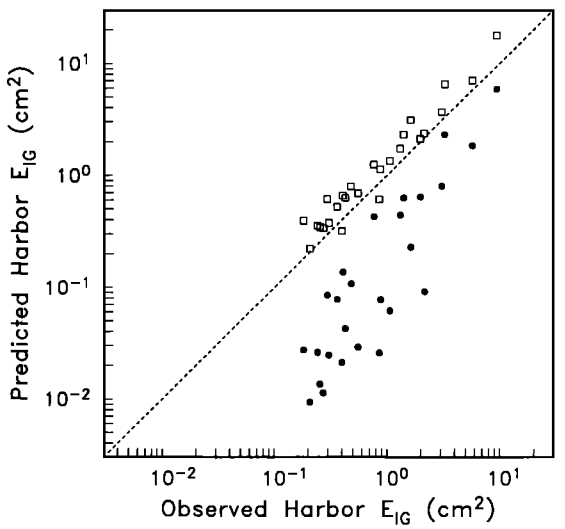

Fig. 15. Predicted versus observed seiche energy for the frequency band $2.0x10^{-3} \leq f < 1.2x10^{-2}$ Hz in the south corner for the 26 records with directional offshore data. Harbor model amplifications ($<A$(south, offshore, f)>; Figure 9) were used to transform offshore infragravity spectra. Squares use observed offshore infragravity spectra (as in Figure 13), and solid circles use the theoretically forced bound infragravity wave spectra, at the offshore location.

spectrum as from the observed offshore infragravity spectrum.

Additional observations with higher energy swell (and presumably increased bound wave dominance offshore; Figure 14) would empirically determine whether the magnitude of the harbor seiche depends primarily on the energy spectrum of pressure fluctuations at infragravity frequencies outside the harbor independently of whether the offshore fluctuations are free or bound. If the sensitivity is low, predictions of harbor seiche for extreme (or design) wave-driven events can be estimated by coupling the predicted bound wave spectrum with the linear seiche model.

Acknowledgments. This work was supported by the U.S. Army Corps of Engineers Civil Research Unit 2219 as part of the Monitoring Completed Coastal Projects Program through the U.S. Army Engineer Waterways Experiment Station, Coastal Engineering Research Center, and by the Coastal Sciences Branch of the Office of Naval Research (contract N00014-89J-1055). Permission was granted by the Chief of Engineers to publish this paper. The staff of the Coastal Data Information Program (supported by the U.S. Army Corps of Engineers and the California Department of Boating and Waterways) installed and maintained the sensors at Barbers Point Harbor. Thanks to T. Herbers and S. Elgar for sharing important results of their ongoing studies of infragravity waves (and their computers); H. Chen for helpful discussions concerning the harbor numerical model; and M. Hemsley, S. Boc, L. Lillycrop, and L. Vincent for their support and assistance. P. Liu and reviewers made helpful comments.

REFERENCES

Berkhoff, J. C. W., Computation of combined refraction-diffraction, *Proc. Int. Conf. Coastal Eng. Conf., 13th*, 471-490, 1972.

Bichkov, V. S., J. Darbyshire, and S. S. Strekalov, The relation between surf beats and wind waves, *Dtsch. Hydrogr. Z., 23*, 165-170, 1970.

Botes, W. A. M., K. S. Russell, and P. Huizinga, Resonance in South African harbours, *Proc. Int. Coastal Eng. Conf., 18th*, 439-453, 1982.

Botes, W. A. M., K. S. Russell, and P. Huizinga, Modeling harbour seiching compared to prototype data, *Proc. Int. Coastal Eng. Conf., 19th*, 846-857, 1984.

Bowers, E. C., Harbour resonance due to set-down beneath wave groups, *J. Fluid Mech., 79*, 71-92, 1977.

Bowers, E. C., Low frequency waves in intermediate depths, *Proc. Int. Coastal Eng. Conf., 23rd*, 832-845, 1992.

Chapman, D. C., and G. S. Giese, A model for the generation of coastal seiches by deep-sea internal waves, *J. Phys. Oceanogr., 20*(9), 1459-1467, 1990.

Chen, H. S., Hybrid element modeling of harbor resonance, *Proc. 4th Int. Conf. on Appl. Numer. Model.*, 312-316, 1984.

Chen, H. S., and C. C. Mei, Oscillations and wave forces in an offshore harbor, *Ralph M. Parsons Lab. Rep. 190*, pp. 1-215, Mass. Inst. of Technol., Cambridge, Mass., 1974.

Clark, D. J., The oscillations of Port Kembla Harbour, *Dock Harbour, 54*(640) 383-384, 1974.

Donn, W. L., and W. T. McGuinness, An investigation of long-period ocean waves, *Int. Union Geodesy Geophys., Monogr. 24*, pp. 26-35, Paris, 1963.

Elgar, S., T. H. C. Herbers, M. Okihiro, J. Oltman-Shay, and R. T. Guza, Observations of infragravity waves, *J. Geophys. Res., 97*(C10), 15,573-15,577, 1992.

Gerber, M., Modelling dissipation in harbour resonance, *Coastal Eng., 10*, 211-252, 1986.

Giese, G. S., and R. B. Hollander, The relationship between coastal seiches at Palawan Island and tide-generated internal waves in the Sulu Sea, *J. Geophys. Res., 92*(C5), 5151-5156, 1987.

Giese, G. S., R. B. Hollander, J. E. Fancher, and B. S. Giese, Evidence of coastal seiche excitation by tide-generated internal solitary waves, *Geophys. Res. Lett., 9*, 1305-1308, 1982.

Giese, G. S., D. C. Chapman, P. G. Black, and J. A. Fornshell, Causation of large-amplitude coastal seiches on the Caribbean coast of Puerto Rico, *J. Phys. Oceanog., 20*(9), 1449-1458, 1990.

Hasselmann, K., On the non-linear energy transfer in a gravity-wave spectrum, 1. General theory, *J. Fluid Mech., 12*, 481-500, 1962.

Herbers, T. C., S. Elgar, R. T. Guza, and W. C. O'Reilly, Infragravity-frequency (0.005-0.05 Hz) motions on the shelf, *Proc. Int. Coastal Eng. Conf., 23rd*, 846-859, 1992.

Horikawa, K., and H. Nishimura, On the function of tsunami breakwaters, *Coastal Eng., 13*, 103-112, 1970.

Houston, J. R., Los Angeles Harbor and Long Beach Harbor: Finite element numerical model of harbor resonance, *Ports '77, 1*, 119-137, 1977.

Houston, J. R., Combined refraction and diffraction of short waves using the finite element method, *Appl. Ocean Res., 3*(4), 163-170, 1981.

Ippen, A. T., and Y. Goda, Wave induced oscillations in harbors: The solution for a rectangular harbor connected to the open-sea, *Tech. Rep 59*, pp. 1-90, Hydrodyn. Lab., Mass. Inst. of Technol., Cambridge, Mass., 1963.

Ito, Y., On the effect of tsunami-breakwater, *Coastal Eng. Jpn., 13*, 89-102, 1970.

Kirkegaard, J., and A. H. Nielsen, Hydraulic studies for Bintulu deepwater port, *Portech 82, 1*, 1-7, 1982.

Kostense, J. K., K. L. Meijer, M. W. Dingemans, A. E. Mynett, and P. vah den Bosch, Wave energy dissipation in arbitrary shaped harbours of

variable depth, *Proc. Int. Coastal Eng. Conf., 20th*, 2002-2016, 1986.
Lee, J.-J., Wave-induced oscillations in harbours of arbitrary geometry, *J. Fluid Mech., 45*, 375-394, 1971.
Lepelletier, T. G., Tsunamis — Harbor oscillations induced by nonlinear transient long waves, *Rep. KH-R-41*, pp. 1-481, W. M. Keck Lab. of Hydraul. and Water Res., Calif. Inst. of Technol., Pasadena, CA., 1980.
Lepelletier, T. G., and F. Raichlen, Harbor oscillations induced by nonlinear transient long waves, *J. Waterw. Port Coastal Ocean Eng., 113*(4), 381-400, 1987.
Lewis, D. P., S. Tsutsui, M. L. Morison, and J. Imberger, Esperance Harbour ship motion study, *Rep. WP-297-DL*, Cent. for Water Res., Univ. of West. Aust., Nedlands, 1989.
Lopez, J. C., and G. G. Pina, Long waves in a Spanish harbour, *Proc. Int. Coastal Eng. Conf., 23rd*, 984-998, 1988.
Matuzawa, T., K. Kanbara, and T. Minakami, Horizontal movement of water in the tsunami of March 3, 1933, *Jpn. J. Astron. Geophys., 11*(1), 11-16, 1933.
Mei, C. C., and Y. Agnon, Long-period oscillations in a harbour induced by incident short waves, *J. Fluid Mech., 208*, 595-608, 1989.
Morison, M. L., and J. Imberger, Water-level oscillations in Esperance Harbour, *J. Waterw. Port Coastal Ocean Eng., 118*(4), 352-367, 1992.
Munk, W. H., Surf beats, *Eos Trans. AGU, 30*(6), 849-854, 1949.
Munk, W. H., F. Snodgrass, and G. Carrier, Edge waves on the continental shelf, *Science, 123*(3187), 127-132, 1956.
Munk, W. H., F. Snodgrass, and F. Gilbert, Long waves on the continental shelf: An experiment to separate trapped and leaky modes, *J. Fluid Mech., 20*, 529-554, 1964.
Okihiro, M., R. T. Guza, and R. J. Seymour, Bound infragravity waves, *J. Geophys. Res., 97*(C7), 11,453-11,469, 1992.
Olsen, K., and L. Hwang, Oscillations in a bay of arbitrary shape and variable depth, *J. Geophys. Res., 76*(21), 5048-5064, 1971.
Panchang, V. G., G. Wei, B. R. Pearce, and M. J. Briggs, Numerical simulation of irregular wave propagation over shoal, *J. Waterw. Port Coastal Ocean Eng., 116*(3), 324-340, 1990.
Rogers, S. R., and C. C. Mei, Nonlinear resonant excitation of a long and narrow bay, *J. Fluid Mech., 88*, 161-180, 1978.
Seymour, R. J., M. H. Sessions, and D. Castel, Automated remote recording and analysis of coastal data, *J. Waterw. Port Coastal Ocean Eng., 111*(2), 388-400, 1985.
Tintoré, J., D. Gomis, S. Alonso, and D.-P. Wang, A theoretical study of large sea level oscillations in the western Mediterranean, *J. Geophys. Res., 93*(C9), 10,797-10,803, 1988.
Tucker, M. J., Surf beats: Sea waves of 1 to 5 minute period, *Proc. R. Soc. London Ser. A, 202*, 565-573, 1950.
Ünlüata, Ü., and C. C. Mei, Effects of entrance loss on harbor oscillations, *J. Waterw. Harbors Coastal Eng. Div., 101*(WW2), 161-180, 1975.
Wilson, B. W., Origin and effects of long period waves in ports., *Proc. 19th Int. Navig. Cong., Sect. II, Commun. 1*, 13-61, 1957.
Wilson, B. W., Tsunami-Responses of San Pedro Bay and Shelf, Calif, *J. Waterw. Harbors Coastal Eng. Div., 97*(WW2), 239-258, 1971.
Wilson, B. W., Seiches, *Adv. Hydrosci., 8*, 1-94, 1972.
Wu, J.-K., and P. L.-F. Liu, Harbour excitations by incident wave groups, *J. Fluid Mech., 217*, 595-613, 1990.
Yamada, N., S. Yamamoto, and Y. Hosokawa, Field observations and analyses of long-period oscillation in harbours and bays, *Coastal Eng. Jpn., 26*, 39-50, 1983.
Zelt, J. A., Tsunamis: The response of harbours with sloping boundaries to long wave excitation, *Rep. KH-R-47*, pp. 1-310, W. M. Keck Lab. of Hydraul. and Water Res., Calif. Inst. of Tech., Pasadena, CA, 1986.

R. T. Guza, M. Okihiro, and R. J. Seymour, Scripps Institution of Oceanography, University of California, San Diego, 9500 Gilman Drive, La Jolla, CA 92093-0222.

(Received March 16, 1993;
revised June 3 1993;
accepted June 15 1993.)